

Computational analysis of the performance of a venturi-shaped roof for natural ventilation: venturi-effect versus wind-blocking effect

B. Blocken *^(a), T. van Hooff^(a,b), L. Aanen^(c), B. Bronsema^(d)

(a) *Building Physics and Systems, Eindhoven University of Technology, P.O. box 513, 5600 MB Eindhoven, the Netherlands*

(b) *Division of Building Physics, Department of Civil Engineering, Katholieke Universiteit Leuven, Kasteelpark Arenberg 40, P.O. Box 2447, 3001 Leuven, Belgium*

(c) *Peutz BV, P.O. box 66, 6585 ZH, Mook, The Netherlands*

(d) *Faculty of Architecture – Department of Climate Design, Delft University of Technology, Prof. Boerhaaveweg 37, 2251 HX Voorschoten, The Netherlands*

Abstract

Computational Fluid Dynamics (CFD) is used to gain insight in the aerodynamic performance of a venturi-shaped roof (called VENTEC roof). The simulations are performed with the 3D steady Reynolds-averaged Navier-Stokes (RANS) equations and the Renormalization Group k- ϵ model. A detailed analysis is conducted of the influence of the so-called venturi-effect and the wind-blocking effect on the aerodynamic performance of the VENTEC roof. The specific roof configuration is intended to create a negative pressure in the narrowest roof section (contraction) which can be used to partly or completely drive the natural ventilation of the building zones. The CFD simulations are based on a detailed grid-sensitivity analysis and on successful validation of the grid-independent results by comparison with experiments in an atmospheric boundary layer wind tunnel. The simulations show that the aerodynamic performance of the roof is governed by the balance between the so-called venturi-effect on the one hand and the wind-blocking effect on the other hand. The venturi-effect cannot act to its full extent because the flow is non-confined. The wind-blocking effect refers to the effect of the resistance exerted by the roof contraction on the air flow and the resulting tendency of the approaching wind to flow around and over the roof, rather than only being forced through the roof contraction. The results indicate that because of the wind-blocking effect, the highest contraction ratio does not provide the best aerodynamic performance and the largest negative pressure, which is a counter-intuitive result. The paper also provides a parametric analysis to optimise the roof contraction height and contraction ratio. The study in this paper illustrates the use of CFD to increase insight in building aerodynamics and to support sustainable building design.

Keywords: Computational Fluid Dynamics (CFD); natural ventilation; venturi-effect; wind-blocking effect; buildings; energy efficiency

1. Introduction

Energy efficiency is an increasingly important design criterion for buildings and urban areas. Natural ventilation or hybrid natural-mechanical ventilation of buildings can be used to provide a comfortable and healthy indoor environment with reduced energy consumption. Natural ventilation is based on either wind-induced pressure differences or thermally-induced pressure differences, or – most often – a combination of both [1-7].

The potential for natural ventilation can be significantly enhanced by the design of the building. Research on natural ventilation of buildings can be performed using different methods [8], including experiments [1,2,5,6,9-17], analytical and/or semi-empirical formulae [1-3,5,15,18,19] and numerical simulation with Computational Fluid Dynamics (CFD) [6,9-13,20-23]. CFD has a number of clear advantages compared with the other approaches (e.g. [24]): (1) as opposed to most experimental techniques, CFD provides whole-flow field data, i.e. data on the relevant parameters in every point of the computational domain; (2) CFD avoids the sometimes incompatible similarity requirements in reduced-scale testing because simulations can be performed at full scale; and (3) CFD allows full control over the boundary conditions and easily and efficiently allows parametric studies

* **Corresponding author:** Bert Blocken, Building Physics and Systems, Eindhoven University of Technology, P.O.Box 513, 5600 MB Eindhoven, the Netherlands. Tel.: +31 (0)40 247 2138, Fax +31 (0)40 243 8595
E-mail address: b.j.e.blocken@tue.nl

to be performed. For these reasons, many studies on evaluating and optimising the natural ventilation potential of buildings have employed CFD (e.g. [6,9-13,20-23]).

Because the roof of a building is often the most exposed part to the oncoming wind, in particular the roof geometry can be employed to enhance natural ventilation. This reasoning has driven the design of a specific venturi-shaped roof by Bronsema in the framework of the research project “Earth, Wind & Fire – Air-conditioning powered by Nature” [7] (Fig. 1). The roof is called the Ventec roof, which is the combination of the Latin word “ventum” (wind) and “tectum” (roof), or the combination of the words “ventilation” and “technology”. The Ventec roof consists of a disk-shaped roof construction that is positioned at a certain height above the actual building, creating a contraction that is expected to provide significant negative pressures due to the so-called Venturi-effect. The negative pressure can be used to partly or completely drive the natural ventilation of the building zones. For this purpose, a vertical channel (not shown in Fig. 1) is provided in the centre of the building, which connects point E of the roof contraction with the building zones at each floor. In a previous paper [23], the present authors have provided a preliminary evaluation of the aerodynamic performance of this roof design by CFD and wind tunnel experiments. At this stage, it was found that adding vertical guiding vanes in the roof contraction actually did not improve but cancelled the effect of the contraction. It was suggested that due to the guiding vanes, the flow resistance through the contraction became too large and that therefore the oncoming wind would flow over and around the roof and the building, rather than being forced to flow between and along the guiding vanes in the contraction. This phenomenon was called the “wind-blocking effect” in earlier studies [23,25-27]. However, this previous study [23] on the venturi-shaped roof did neither investigate the wind-blocking effect in detail, nor did it provide an optimisation analysis of the roof contraction height and contraction ratio. These two effects and the optimisation analysis are interrelated and they are the main focus of the present paper.

In the present study, 3D steady Reynolds-averaged Navier-Stokes (RANS) CFD with the Renormalization Group (RNG) $k-\epsilon$ model is used to investigate the balance between the so-called venturi-effect and the wind-blocking effect for flow through and around the venturi-shaped roof and to determine the optimum contraction height. RANS CFD requires turbulence modelling, which in turn requires solution verification and validation studies. Therefore, the study also contains a detailed grid-sensitivity analysis and a validation study based on comparison of the grid-independent simulation results with a set of experiments in an atmospheric boundary layer wind tunnel. Next, the validated CFD model is used for a series of parametric CFD simulations that allow (1) optimising the aerodynamic performance of the roof in terms of the roof contraction height and (2) investigating the balance between the venturi-effect and the wind-blocking effect.

2. Venturi-effect and wind-blocking effect

In this section, the venturi-effect and the wind-blocking effect are briefly addressed. The venturi-effect refers to the increase of the fluid speed due to a decrease of the flow cross-section [27,28]. This effect was originally defined for confined flows [28], but the same terminology has been used for non-confined flow or open flows, e.g. to describe the increase of wind speed in passages between buildings [29-31]. Recent research however has shown that in a passage between two buildings, the venturi-effect is – at least in some cases – not the governing effect [25-27]. Indeed, as the passage width decreases, the resistance for flow through the passage increases and more wind will flow around and over the building passage, rather than being forced to flow through it. Blocken et al. [25-27] referred to this as the “wind-blocking effect”: the high resistance of the passage partly blocks the flow through the passage and diverts a large part of the oncoming wind over and around the buildings and the passage. This is an explicit characteristic of non-confined flows, and therefore the term venturi-effect is less suitable here [25,27]. A detailed analysis in terms of average wind speed and wind fluxes was performed, confirming that – at least for the building configurations under investigation – the so-called venturi-effect was not present, because it was overruled by the wind-blocking effect [25-27]. Figure 2 illustrates results of this previous study for buildings in a so-called converging arrangement. In the past, this arrangement has been called “venturi-throat”. The presence of the venturi-effect would at least imply that the fluxes (flow rates) through the passage plane are higher than the free-field flux through a similar plane in the upstream undisturbed flow. However, the previous CFD study, validated by wind tunnel experiments, has shown that the flow rates through these “converging” building passages are consistently lower than the corresponding free-field flow rates, irrespective of the passage width (Fig. 2a). This implies that the term venturi-effect is not really applicable for such building configurations. Therefore, as a general rule for non-confined flows, the term venturi-effect should be used with caution, because it is not known in advance to which extent this effect will be overruled by the wind-blocking effect. Figure 2b shows that the wind-blocking effect causes an uplift of the approaching flow and part of it therefore flows over the buildings and the passage and not through the passage.

The flow through and around the Ventec roof in the present study is also a non-confined flow. Similar to the case of the two-building configuration in [25-27], the resulting wind flow through the roof will be influenced by the resistance of the contraction. In the next sections, the balance between the venturi-effect (due to roof

contraction) and the wind-blocking effect (due to resistance caused by roof contraction) will be analysed for the building in Fig. 1 with varying contraction height c . Note that in this paper, we will use the term “venturi-effect” to refer to the expected increase of flow speed and negative pressure in the contraction, in spite of the non-confined flow conditions.

3. Description of building and roof geometry

Fig. 1 illustrates the geometry under study. The building has a rectangular (20 m x 20 m) floor plan and a height of 50 m, measured up to the edge of the roof. The Ventec roof consists of two parts. The lower part is constructed from half a “square disk” with dimensions 23.4 m x 23.4 m x 2 m (L x W x H) and it is positioned directly on top of the building, this way creating a roof overhang of 1.7 m on each side of the building, at which ventilation inlets will be placed. At a distance ‘ c ’ (contraction height) above this part of the roof a “full square disk” is positioned with dimensions 23.4 m x 23.4 m x 4 m (L x W x H), resulting in a nozzle-shaped roof entrance from all four sides of the building. This part can be supported by a set of slender vertical columns, as indicated in Fig. 1a. In this study, the contraction height c (and therefore also the inlet height b) will be varied by vertically translating the “full square disk” and increasing the distance b and c with the same translation distance. Therefore, the geometry of the building and the square disk itself will not change. The values of the parameter c and the corresponding values of the parameter b and the contraction ratio b/c are given in Table 1.

The position of interest inside the roof contraction is the point in the bottom centre of the roof, indicated with the letter E (from “exhaust”) in Figure 1a and b. In this study, the exhaust is considered to be closed and the surface pressure at this position will be evaluated. A reasonable expectation is that at this position, the flow speed will reach a maximum value and that also the resulting absolute value of the negative pressure will reach a maximum value.

All experiments and simulations are conducted for an isolated building, i.e. without surrounding buildings. Therefore, all differences in wind speed and surface pressures between the different configurations are only due to changes in the parameter c .

4. Wind tunnel measurements

A reduced-scale model (1:100) of the building with Ventec roof is constructed and placed in the closed-circuit atmospheric boundary layer (ABL) wind tunnel (Fig. 3) at Peutz BV in Mook, the Netherlands. The dimensions of the wind tunnel test section are 3.2 x 1.8 m² (W x H), resulting in a blockage ratio of about 2%. The building model was placed on a turntable with a diameter of 2.3 m. Part of the measurements were reported in the previous paper [23]. In the present paper, additional measurement results for different values of the parameter c are reported. The surface pressure was measured at the position E (Fig. 1) with a HCLA12X5EB amplified differential pressure sensor from SensorTechnics. The wind speed in the roof contraction was measured in the centre of the contraction, at mid-height, using a NTC resistor element. The NTCs are operated with a constant current and are calibrated by Peutz by determining the relationship between wind speed and temperature (and corresponding resistance) of each individual probe. The probes are not direction-sensitive and due to the relatively long reaction time of the probes, only average wind speeds can be measured, with an accuracy of $\pm 10\%$. Approach-flow vertical profiles of mean wind speed U and turbulence intensity I_u are measured at the edge of the turntable using hot-wire anemometers and are presented in Figure 4. The measured wind speed profile can be described by a logarithmic law with a friction velocity $u^* = 0.956$ m/s and an aerodynamic roughness length $y_0 = 0.005$ m (full scale: $y_0 = 0.5$ m). The incident reference wind speed at roof height (full scale: 50 m) is 10.5 m/s. Measurements are made for four wind directions: $\varphi = 0^\circ, 15^\circ, 30^\circ$ and 45° , taking into account the symmetry of the building and the building roof.

5. CFD simulations: geometry, grid, boundary conditions and solver settings

5.1. Computational geometry and grid

After having verified that the results are Reynolds number independent and that simulations at model scale therefore yield similar results as simulations at full scale [23], all other simulations were performed at model scale. For clarity however, all parameter and results will be expressed with full-scale values. The computational domain has (full-scale) dimensions L x B x H = 1020 m x 1020 m x 300 m (Fig. 5a). This domain shape allows modelling different wind directions (0° to 45°). High-quality and high-resolution computational grids were constructed (Fig. 5 and Fig. 6). The grids have at least 10 cells between each two adjacent surfaces as requested by the best practice guidelines by Franke et al. [32] and Tominaga et al. [33]. The grids are made using the grid generation technique presented by van Hooff and Blocken [6]. In this technique, the geometry and the grid are created simultaneously, by a series of extrusion operations. This procedure allows a large degree of control over

the size and shape of the cells, and therefore of the quality and resolution of the computational grid. It allows high-quality grids to be made, even for rather complex geometries. The same technique has been used successfully on previous occasions to model sport stadium geometries [6,22,34]. The grids are block-structured. The number of cells for every configuration (c value) is between about 2.0 and 2.3 million cells. Note that the grids do not contain any pyramidal or tetrahedral cells. Special attention was paid to the detailed reproduction and meshing of the wind roof geometry. A high grid resolution is applied in the proximity of the roof in view of the expected large flow gradients (Fig. 6 and 7). A detailed grid-sensitivity analysis was performed indicating that the grid resolution shown in Figure 6c provides nearly grid-independent results. The grid-sensitivity analysis will be reported in section 6.1.

5.2. Boundary conditions

At the inlet of the domain the measured approach-flow mean wind speed profile is imposed. Turbulent kinetic energy k is calculated from the turbulence intensity I_u using $k = 0.5(I_u U)^2$. The turbulence dissipation rate $\varepsilon = (u^*)^3/\kappa(y+y_0)$, where y is the height coordinate, κ the von Karman constant ($\kappa = 0.42$) and u^* the friction velocity related to the logarithmic mean wind speed profile. At the ground and building surfaces, the standard wall functions by Launder and Spalding [35] are used with the sand-grain based roughness modification by Cebeci and Bradshaw [36]. For the ground surface, the parameters k_S and C_S , to be used in Fluent [37] should be selected to correctly represent the rough fetch upstream of the building model (see Fig. 3a). This type of consistent atmospheric boundary layer simulation is very important to obtain accurate simulation results [25,38]. Therefore, k_S and C_S have to be determined using their appropriate consistency relationship with y_0 . This relationship was derived by Blocken et al. [38] for Fluent and CFX. For Fluent 6, up to at least version 6.3, it is given by $k_S = 9.793y_0/C_S$. The combination $k_S = 0.98$ m and $C_S = 5$ is selected (see Fig. 5). The building surfaces are assumed to be smooth ($k_S = 0$ m and $C_S = 0.5$). Zero static pressure is imposed at the outlet of the domain and the top of the domain is modelled as a slip wall (zero normal velocity and zero normal gradients of all variables).

5.3. Solver settings

The 3D steady RANS equations are solved in combination with the RNG k - ε turbulence model [39] using Fluent 6.3.26. The RNG k - ε turbulence model was chosen because of its good performance in predicting the surface pressures on the windward building facades and in the roof opening in a preliminary study [23] and because of its superior performance in an earlier study by Evola and Popov [40]. Pressure-velocity coupling is taken care of by the SIMPLE algorithm, pressure interpolation is standard and second-order discretization schemes are used for both the convection terms and the viscous terms of the governing equations. Convergence has been monitored carefully and the iterations have been terminated when all scaled residuals showed no further reduction with increasing number of iterations. At this stage, the scaled residuals [37] were: 10^{-4} for continuity, 10^{-7} for momentum, 10^{-6} for turbulent kinetic energy and 10^{-4} for turbulence dissipation rate.

6. Grid-sensitivity analysis, experimental validation and optimisation results

6.1. Grid-sensitivity analysis

A grid-sensitivity analysis was performed by constructing two additional grids for the configuration with $c = 1$ m: a coarser grid and a finer grid (Fig. 6 and 7). Coarsening and refining was performed with an overall linear factor $\sqrt{2}$. The coarse grid has 549,380 cells, the middle grid has 2,041,268 cells and the fine grid has 4,364,688 cells. These grids are shown in Fig. 6b-d and Fig. 7a-c. The results on the three grids are compared in Figure 8 in terms of the absolute values of the mean pressure coefficients on the windward building facade and at position E in the roof contraction. The pressure coefficients are computed as $C_p = (P - P_0)/(0.5\rho U_{ref}^2)$ with P the static pressure at the surface, P_0 the reference static pressure, $\rho = 1.225$ kg/m³ the air density and U_{ref} the reference wind speed at roof height ($U_{ref} = 10.5$ m/s at $y = 0.5$ m). A small deviation (7 %) is found between the coarse and middle grid for the C_p at position E, while almost no deviation is found for the value of this parameter between the middle grid and the fine grid. Therefore, the middle grid (i.e. that in Fig. 6c) is retained for further analysis, and the grids for the other c values are constructed with similar grid resolution.

6.2. Experimental validation

Validation is performed by comparing the CFD simulation results with the wind tunnel measurements. Figure 9 compares the numerically simulated and measured mean pressure coefficients C_p at position E in the centre of the roof contraction. The CFD results and the wind tunnel results are in fairly good agreement. The agreement however seems to deteriorates for the lower c values. These deviations can be attributed to: (1) the specific

geometry of the roof, with four “ribs” on the roof surfaces (see e.g. Fig. 1a); (2) the fact that the vertical roof supports were not included in the numerical model; and (3) the large C_p gradients at the roof surfaces, which are more pronounced for lower c values. In spite of these deviations between the numerical and the measured C_p values, the trends are clear and allow a comparison of the performance of the different roof configurations. Figure 10 compares the numerically simulated and measured mean wind speed ratios U/U_{ref} at mid-height in the centre of the roof contraction, for the three configurations ($c = 0.5$ m, $c = 1$ m and $c = 2$ m) and for the four wind directions. The deviations are generally smaller than 10%, which is considered a very close agreement.

6.3. Optimisation results

Based on the grid-sensitivity analysis and the validation study, CFD simulations are performed to determine the mean C_p at position E for different values of the contraction height c . Figure 11 shows that a maximum (negative) value is obtained for $c = 0.5$ m. The existence of this optimal value is the result of the balance between the so-called venturi-effect and the wind-blocking effect. This will be examined in more detail in the next section.

7. Analysis of venturi-effect versus wind-blocking effect

A detailed analysis of the flow rates and average wind speeds through different cross-sections of the roof is performed for wind direction $\varphi = 0^\circ$. Figure 12a defines the line segment L_1 in the middle of the roof contraction. Fig. 12b defines the vertical bounded planes A_1 , A_2 , A_3 and A_6 and the corresponding air flow rates F_1 , F_2 , F_3 and F_6 through these planes. A_1 is situated in the upstream undisturbed flow and represents “free-field” conditions. A_2 is the “roof contraction inlet” plane. A_3 is the “roof contraction middle plane” and A_6 is the “roof contraction outlet” plane. Note that the areas of A_1 , A_2 and A_6 are the same, while the area of A_3 is smaller, due to the specific roof geometry/contraction. Figure 12c defines two additional bounded planes A_4 and A_5 , which correspond to the side openings of the roof and which have the same area as A_1 . The corresponding air flow rates are F_4 and F_5 . Note that Fig. 12 only shows the configuration for one value of the parameter c ($c = 1$ m). For a given configuration (and value of the parameter c), the areas of the bounded planes A_1 , A_2 , A_4 , A_5 and A_6 are the same. However, these areas vary with c .

Figure 13 illustrates how the ratio F_2/F_1 decreases with decreasing contraction height c . The smaller c , the larger the resistance in the roof contraction (more wind-blocking) and the smaller the ratio of the air flow rate entering the roof contraction (through A_2) to the free-field air flow rate (through A_1).

Figure 14 shows two curves. The first one indicates the decrease of the ratio F_6/F_2 (outlet flow rate to inlet flow rate) with decreasing value of c . The second one shows the increase of the ratio $(F_4 + F_5)/F_2$ (side flow rate to inlet flow rate) with decreasing c . The sum of the two curves is equal to one. These curves indicate that the smaller the contraction height, the larger the resistance and the wind-blocking effect. Due to the wind-blocking effect, a larger fraction of the air that enters the roof will exit through the side planes A_4 and A_5 instead of through the exit plane A_6 . This is further clarified in Fig. 15, that shows the velocity vector field in a horizontal plane through the middle of the roof contraction, for $c = 0.25$ and $c = 2$ m. Fig. 15a shows a strong lateral deviation of wind flow in the roof for $c = 0.25$ m, which is much less pronounced for $c = 2$ m. Fig. 16 shows the velocity vector field in the vertical centre plane for $c = 0.25$ and $c = 2$ m. Comparing Fig. 16a and b clearly shows the much stronger exit flow in the case with larger c value. Comparing Fig. 16c and d also shows larger vertical velocity components upstream of the roof inlet, indicating that the wind-blocking forces more of the air to flow over the roof rather than only through it.

Finally, Fig. 17 illustrates curves for two average velocity ratios, in which the average velocity is calculated as the flow rate through the bounded plane divided by the area of the bounded plane, or as the average values of the velocities along the vertical line segment L . The first ratio U_{A3}/U_{A2} is the average velocity through area A_3 (vertical contraction middle plane) to the average velocity through area A_2 (vertical contraction inlet plane). The second ratio U_{L1}/U_{A2} is the average velocity along line segment L_1 to U_{A2} . Both curves illustrate the balance between the venturi-effect and the wind-blocking effect, in which this balance yields a maximum velocity ratio for $c = 0.5$ m. For lower c values, the higher contraction ratio yields a stronger wind-blocking effect and the ratios decrease. For higher c values, the lower contraction ratio yields a less strong venturi-effect. The fact that the ratio U_{L1}/U_{A2} is always larger than U_{A3}/U_{A2} is a direct consequence of the shape of the roof contraction and indicates that position E is indeed a good position for a ventilation outlet.

8. Discussion

This study has evaluated the balance between the so-called venturi-effect and the wind-blocking effect in the aerodynamic performance of a venturi-shaped roof (called the Ventec roof) for wind-induced natural ventilation of buildings. The study has built further on a previous investigation which included evaluating the effect of

vertical guiding vanes in the contraction [23]. This previous study had shown that adding guiding vanes has a strong negative effect on the aerodynamic performance of the roof, which was attributed to the wind-blocking effect that overruled the venturi-effect.

Therefore, the present study has investigated the venturi-effect and the wind-blocking effect in detail. It has also investigated the optimum contraction height. While the study has provided new insights in the aerodynamic performance of the Ventec roof, the study also has some important limitations. It has focused on only one building geometry ($L \times B \times H = 20 \text{ m} \times 20 \text{ m} \times 50 \text{ m}$), one roof geometry (square disk of $23.4 \text{ m} \times 23.4 \text{ m}$ with 4 m maximum thickness) and – for the largest part – also only one wind direction. The study did also not explicitly include the effect of surrounding buildings. Finally, also the exhaust air flow coming from the building zones and being extracted by the generated negative pressure was not modelled. Therefore, it is possible that in a real situation the optimum contraction height (and contraction ratio) will be somewhat different. Nevertheless, in spite of these limitations, this study has clarified the two main aerodynamic effects that determine the aerodynamic performance of the Ventec roof: the so-called venturi-effect and the wind-blocking effect. These two effects should also be considered in future optimisation studies for different building and roof geometries, different surroundings and exhaust air flow rates.

Note that we have chosen to present the results in this paper as a function of the actual contraction height c , rather than as a function of a normalised/dimensionless contraction height value. The reason is that it is not yet clear which geometrical parameter is a suitable length scale for normalisation. Ideally, such a length scale would need to somehow represent both the dimensions of the roof and the dimensions of the building, because both set of dimensions are expected to play an important role in the aerodynamic performance of the roof. This is a topic of further analysis in future studies.

The evaluation of the aerodynamic performance of the roof has been mainly conducted based on the value of the negative pressure coefficient at point E. However, as mentioned in section 6.2, large pressure gradients are present in the roof contraction. Point E was chosen because of its position in the centre of the contraction, and because it corresponded to the location of the point measurement in the wind tunnel model. A future study on the aerodynamic performance of the roof will include modelling the exhaust flow rate through the vertical channel, and that enters the roof contraction due to the generated negative pressure.

9. Conclusions

This paper has presented a computational analysis of the aerodynamic performance of a venturi-shaped roof for natural ventilation of buildings, from the viewpoint of the two main governing effects: the so-called venturi-effect and the wind-blocking effect. The analysis has been performed with 3D steady Reynolds-averaged Navier-Stokes (RANS) CFD simulations with closure by the Renormalisation Group $k-\epsilon$ model. The CFD simulations have been based on a detailed grid-sensitivity analysis and on successful validation of the grid-independent results by comparison with experiments in an atmospheric boundary layer wind tunnel.

The aerodynamic performance of the roof has been evaluated in terms of the mean negative pressure generated in the narrowest part of the contraction. This negative pressure can be used to drive the natural ventilation of the building zones. The performance of the roof is determined by the balance between the so-called venturi-effect and the wind-blocking effect. Note that this paper has used the adjective “so-called” for venturi-effect because this effect strictly refers to confined flows, which is not the case in the present study. The wind-blocking effect refers to the resistance exerted by the roof contraction on the air flow and the resulting tendency of the approaching wind to flow around and over the roof, rather than only being forced through the roof.

The study has shown that due to the wind-blocking effect, the negative pressure in the roof does not monotonically decrease with increasing contraction height and that an optimum contraction height exists. The reason is that a smaller contraction height leads to a higher resistance for flow through the contraction, which causes more of the approaching wind to flow over and around the roof rather than through its narrow contraction. Due to this wind-blocking effect, the highest contraction ratio does not provide the best aerodynamic performance and the largest mean negative pressure, which is a counter-intuitive result.

The study in this paper has illustrated the use of CFD to increase insight in building aerodynamics and to support sustainable building design.

References

- [1] Linden PF. The fluid mechanics of natural ventilation. *Annu Rev Fluid Mech* 1999;31: 201-238.
- [2] Hunt GR, Linden PF. The fluid mechanics of natural ventilation - displacement ventilation by buoyancy-driven flows assisted by wind. *Build Environ* 1999;34(6): 707-720.
- [3] Li YG, Delsante A. Natural ventilation induced by combined wind and thermal forces. *Build Environ* 2001;36(1): 59-71.

- [4] Khan N, Su Y, Riffat SB. A review on wind driven ventilation techniques. *Energy Build* 2008;40(8), 1586-1604.
- [5] Larsen TS, Heiselberg P. Single-sided natural ventilation driven by wind pressure and temperature difference. *Energy Build* 2008;40(6): 1031-1040.
- [6] van Hooff T, Blocken B. Coupled urban wind flow and indoor natural ventilation modelling on a high-resolution grid: A case study for the Amsterdam ArenA stadium. *Environ Modell Softw* 2010;25(1): 51-65.
- [7] Bronsema B. Earth, Wind & Fire – Air-conditioning powered by nature. 10th REHVA World Congress CLIMA 2010, 9-12 May, Antalya, Turkey.
- [8] Chen Q. Ventilation performance prediction for buildings: A method overview and recent applications. *Build Environ* 2009;44(4) 848-858.
- [9] Kato S, Murakami S, Mochida A, Akabayashi Shin-ichi, Tominaga Y. Velocity-pressure field of cross ventilation with open windows analyzed by wind tunnel and numerical simulation. *J Wind Eng Ind Aerod* 1992;44(1-3): 2575-2586.
- [10] Kato S, Murakami S, Takahashi T, Gyobu T. Chained analysis of wind tunnel test and CFD on cross ventilation of large-scale market building. *J Wind Eng Ind Aerod* 1997;67-68: 573-587.
- [11] Jiang Y, Alexander D, Jenkins H, Arthur R, Chen Q. Natural ventilation in buildings: Measurement in a wind tunnel and numerical simulation with large-eddy simulation. *J Wind Eng Ind Aerod* 2003;91(3) 331-353.
- [12] Heiselberg P, Li Y, Andersen A, Bjerre M, Chen Z. Experimental and CFD evidence of multiple solutions in a naturally ventilated building. *Indoor Air* 2004;14(1): 43-54.
- [13] Gao NP, Niu JL, Perino M, Heiselberg P. The airborne transmission of infection between flats in high-rise residential buildings: Tracer gas simulation. *Build Environ* 2008;43(11): 1805-1817.
- [14] Tablada A, de Troyer F, Blocken B, Carmeliet J, Verschure H. On natural ventilation and thermal comfort in compact urban environments - the Old Havana case. *Build Environ* 2009;44(9): 1943-1958.
- [15] Karava P, Stathopoulos T, Athienitis AK. Wind-induced natural ventilation analysis. *Sol Energy* 2007;81(1): 20-30.
- [16] Bu Z, Kato S, Takahashi T. Wind tunnel experiments on wind-induced natural ventilation rate in residential basements with areaway space. *Build Environ* 2010;45(10): 2263-2272.
- [17] Karava P, Stathopoulos T, Athienitis AK. Airflow assessment in cross-ventilated buildings with operable facade elements. *Build Environ* 2011;46(1): 266-279.
- [18] Costola D, Blocken B, Hensen JLM. Overview of pressure coefficient data in building energy simulation and airflow network programs. *Build Environ* 2009;44(10): 2027-2036.
- [19] Costola D, Blocken B, Ohba M, Hensen JLM. Uncertainty in airflow rate calculations due to the use of surface-averaged pressure coefficients. *Energy Build* 2010;42(6): 881-888.
- [20] Norton T, Grant J, Fallon R, Sun DW. Assessing the ventilation effectiveness of naturally ventilated livestock buildings under wind dominated conditions using computational fluid dynamics. *Biosystems Engineering* 2009;103(1): 78-99.
- [21] Norton T, Grant J, Fallon R, Sun DW. Optimising the ventilation configuration of naturally ventilated livestock buildings for improved indoor environmental homogeneity. *Build Environ* 2010;45(4): 983-995.
- [22] van Hooff T, Blocken B. On the effect of wind direction and urban surroundings on natural ventilation of a large semi-enclosed stadium. *Comput Fluids* 2010;39(7): 1146-1155.
- [23] van Hooff T, Blocken B, Aanen L, Bronsema B. A venturi-shaped roof for wind-induced natural ventilation of buildings: wind tunnel and CFD evaluation of different design configurations. *Build Environ* 2011. In press. doi:10.1016/j.buildenv.2011.02.009
- [24] Blocken B, Stathopoulos T, Carmeliet J, Hensen JLM. Application of CFD in building performance simulation for the outdoor environment: an overview. *Journal of Building Performance Simulation* 2011; in press. doi: 10.1080/19401493.2010.513740
- [25] Blocken B, Carmeliet J, Stathopoulos T. CFD evaluation of the wind speed conditions in passages between buildings – effect of wall-function roughness modifications on the atmospheric boundary layer flow. *J Wind Eng Ind Aerod* 2007;95(9-11): 941-962.
- [26] Blocken B, Stathopoulos T, Carmeliet J. Wind environmental conditions in passages between two long narrow perpendicular buildings. *J Aerospace Eng-ASCE* 2008;21(4): 280-287.
- [27] Blocken B, Stathopoulos T, Carmeliet J. A numerical study on the existence of the Venturi-effect in passages between perpendicular buildings. *J Eng Mech-ASCE* 2008;134(12): 1021-1028.
- [28] Venturi GB. Experimental enquiries concerning the principle of the lateral communication of motion in fluids: applied to the explanation of various hydraulic phenomena. 1799. Translated from the French by Nicholson W, 1st English ed., J. Taylor, Architectural Library, High-Holborn, London.
- [29] Gandemer J. Wind environment around buildings: aerodynamic concepts. Proc., 4th Int. Conf. Wind Effects on Buildings and Structures, Heathrow 1975, Cambridge University Press, 423-432.
- [30] Lawson TV. Wind effects on buildings, Vol. 1, 1980, Applied Science Publishers Ltd., London, England.

- [31] Dutt AJ. Wind flow in an urban environment. *Environ. Monit. Assess.* 1991;19(1-3): 495-506.
- [32] Franke J, Hellsten A, Schlünzen H, Carissimo B (Eds.). Best practice guideline for the CFD simulation of flows in the urban environment. COST Office Brussels; 2007.
- [33] Tominaga Y, Mochida A, Yoshie R, Kataoka H, Nozu T, Yoshikawa M, Shirasawa T. AIJ guidelines for practical applications of CFD to pedestrian wind environment around buildings. *J Wind Eng Ind Aerod* 2008;96(10-11): 1749-61.
- [34] van Hooff T, Blocken B, van Harten M. 3D CFD simulations of wind flow and wind-driven rain shelter in sports stadia: influence of stadium geometry. *Build Environ* 2011;46(1): 22-37.
- [35] Launder BE, Spalding DB, The numerical computation of turbulent flows. *Comput Method Appl M* 1974;3: 269-289.
- [36] Cebeci T, Bradshaw P. Momentum transfer in boundary layers, Hemisphere Publishing Corporation; 1977.
- [37] Fluent Inc. Fluent 6.3. User's Guide. Fluent Inc., Lebanon; 2006.
- [38] Blocken B, Stathopoulos T, Carmeliet J. CFD simulation of the atmospheric boundary layer: wall function problems. *Atmos Environ* 2007;41(2): 238-252.
- [39] Yakhot V, Orszag SA, Thangam S, Gatski TB, Speziale CG. Development of turbulence models for shear flows by a double expansion technique. *Physics of Fluids* 1992;A4: 1510-1520.
- [40] Evola G, Popov V. Computational analysis of wind driven natural ventilation in buildings. *Energy Build* 2006;38(5): 491-501.

Table 1. Parameters c (contraction height), b and b/c (contraction ratio) for the six different configurations.

c (m)	0.25	0.375	0.5	0.75	1	2
b (m)	4.25	4.375	4.5	4.75	5	6
b/c	17.0	11.7	9.0	6.3	5.0	3.0

FIGURES

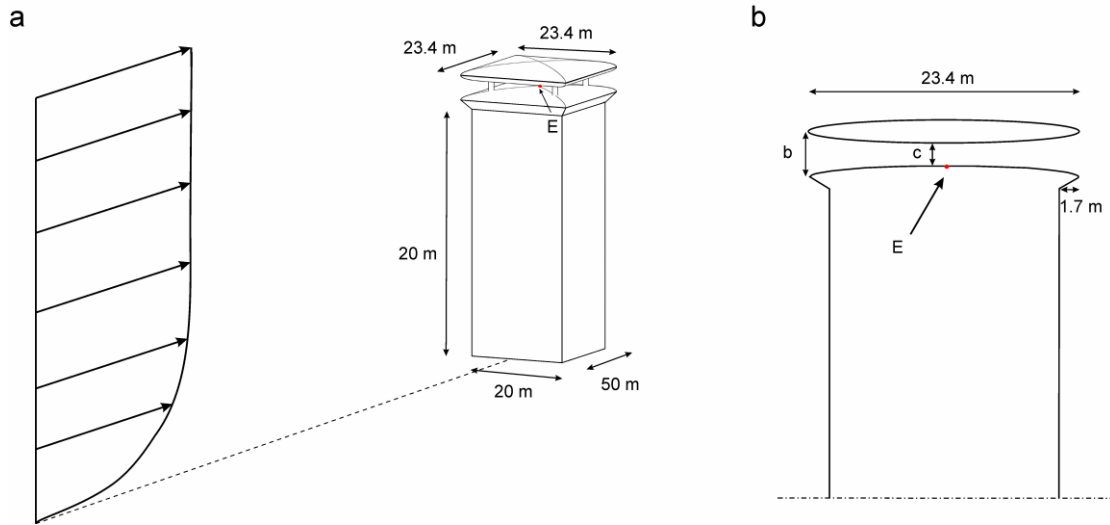


Figure 1: (a) Perspective view of the building with venturi-shaped roof (Ventec roof) and main dimensions. (b) Vertical cross-section of the building and Ventec roof with indication of parameters b and c and position E where the surface pressure is evaluated.

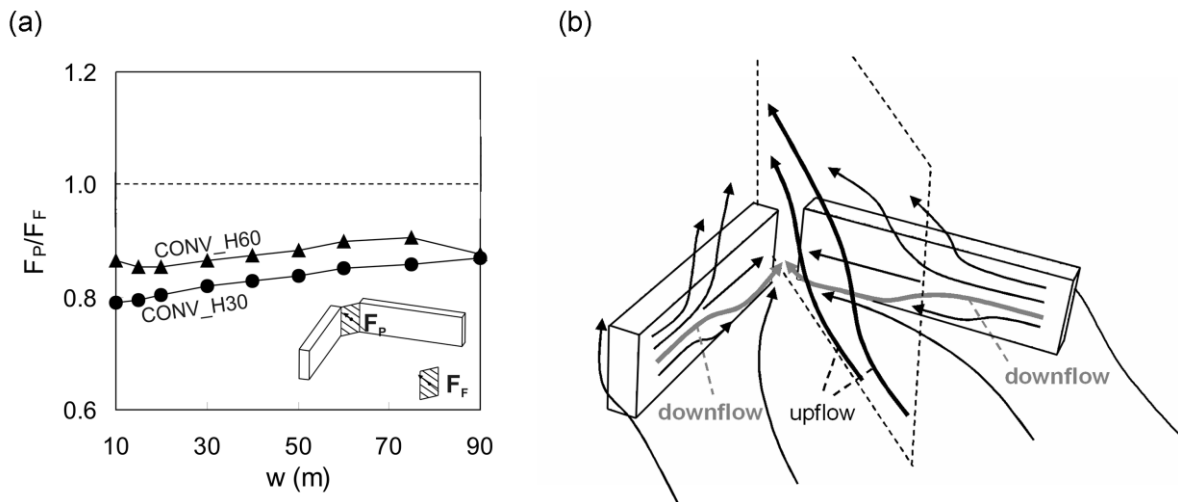


Figure 2: Illustration of the wind-blocking effect for a converging arrangement of two high-rise buildings (a) Ratio of the passage flux F_P to the free-field flux F_F for buildings with height $H = 30$ m and $H = 60$ m, and for different passage widths w (from [26]). (b) Schematic representation of flow in the converging passage with $H = 30$ m and $w = 10$ m. The vertical plane cuts midway through the passage. The upflow due to the wind-blocking effect is responsible for the fact that the ratio F_P/F_F is smaller than 1 (from ([26])).

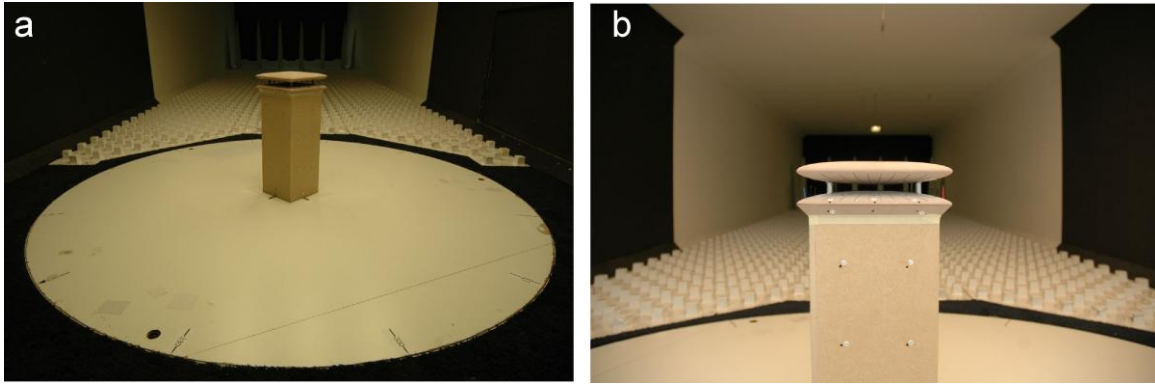


Figure 3: Pictures of the reduced-scale building model with Ventec roof in the closed-circuit ABL wind tunnel at Peutz BV. (a) View of the upstream domain with building model positioned in the middle of the turntable for wind direction of 45°. (b) Close-up view of the building model with Ventec roof.

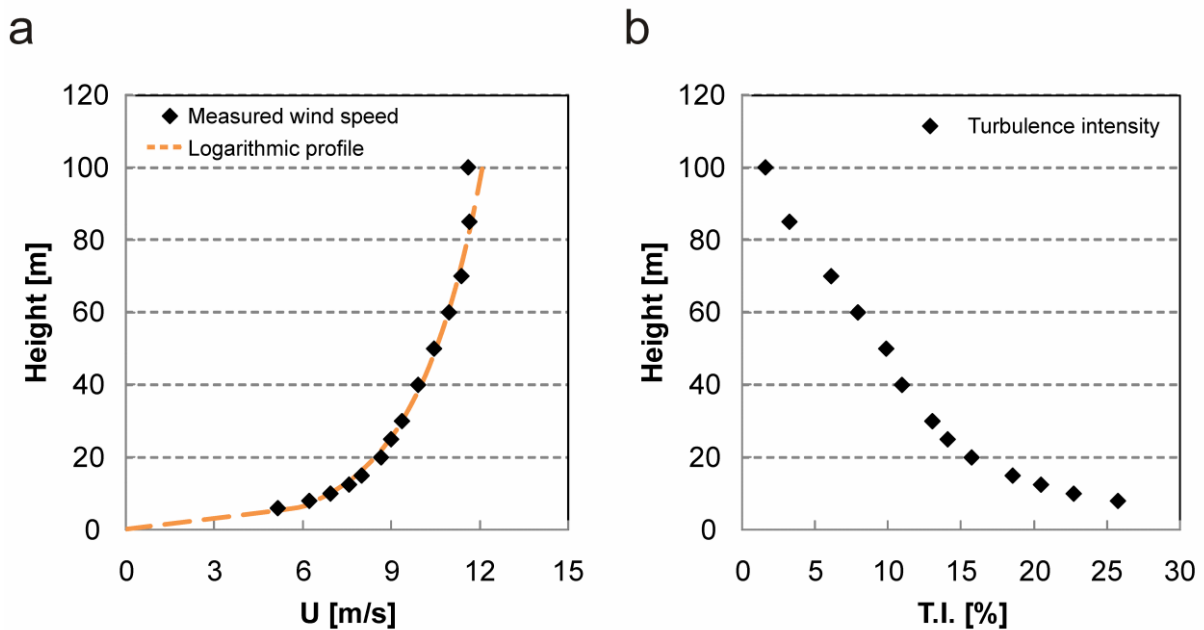


Figure 4: (a) Measured approach-flow mean wind speed profile along a vertical line at the upstream edge of the turntable (full-scale dimensions; log law profile with $u^* = 0.956$ m/s and $y_0 = 0.5$ m). (b) Measured turbulence intensity T.I. along the same vertical line (full-scale dimensions).

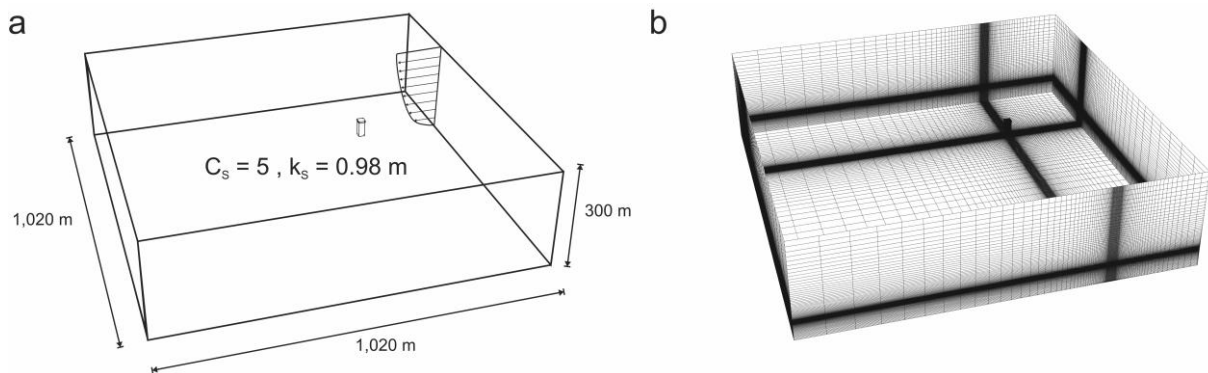
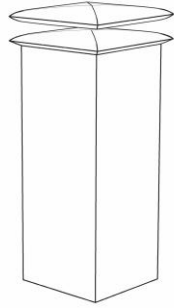
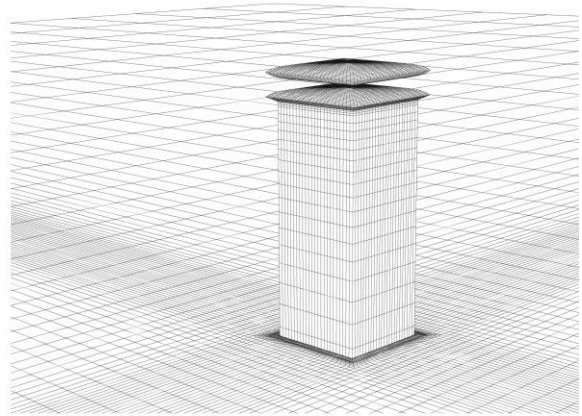


Figure 5: (a) Perspective view of the building in its computational domain (full-scale dimensions and parameter values). (b) View of the computational grid at the building and some of the domain surfaces.

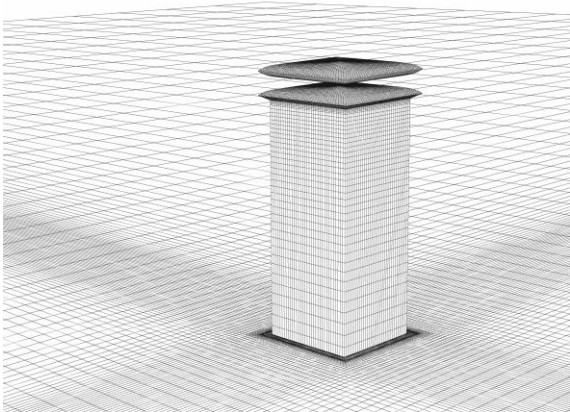
a



b



c



d

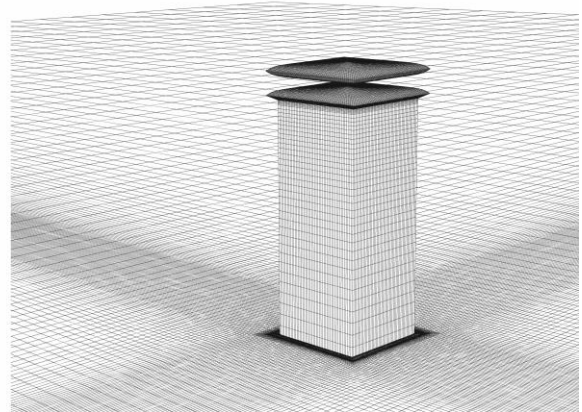


Figure 6. Geometry and perspective view of computational grids for configuration with $c = 1$. (a) Geometry. (b-d) Computational grids used for the grid-sensitivity analysis: (b) coarse grid (549,380 cells); (c) middle grid (2,041,268 cells); (d) fine grid (4,364,688 cells).

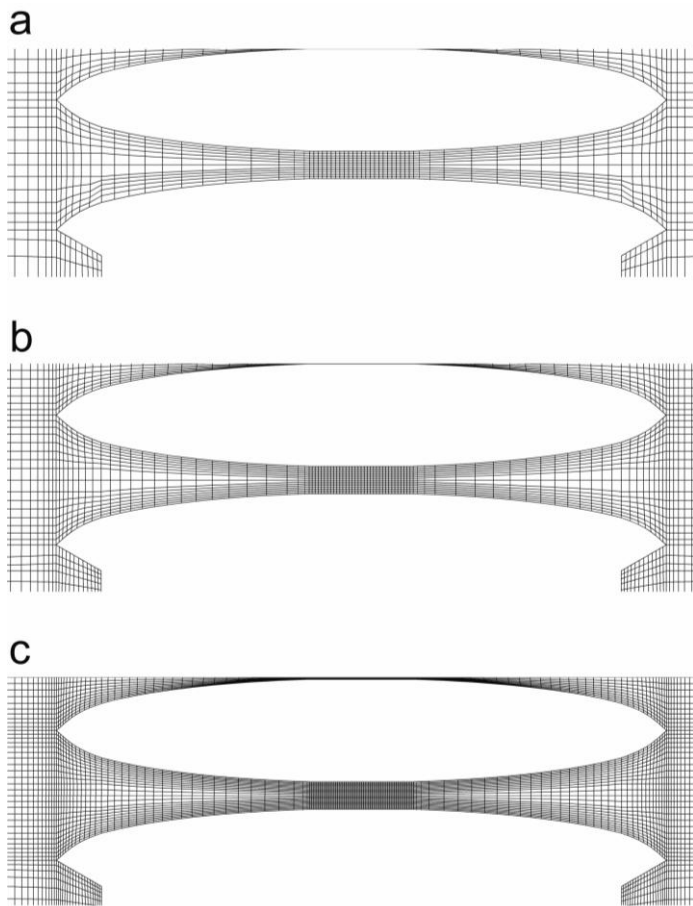


Figure 7. Computational grids in the vertical cross-section of the roof contraction for configuration with $c = 1$. (a) coarse grid (549,380 cells); (b) middle grid (2,041,268 cells); (c) fine grid (4,364,688 cells).

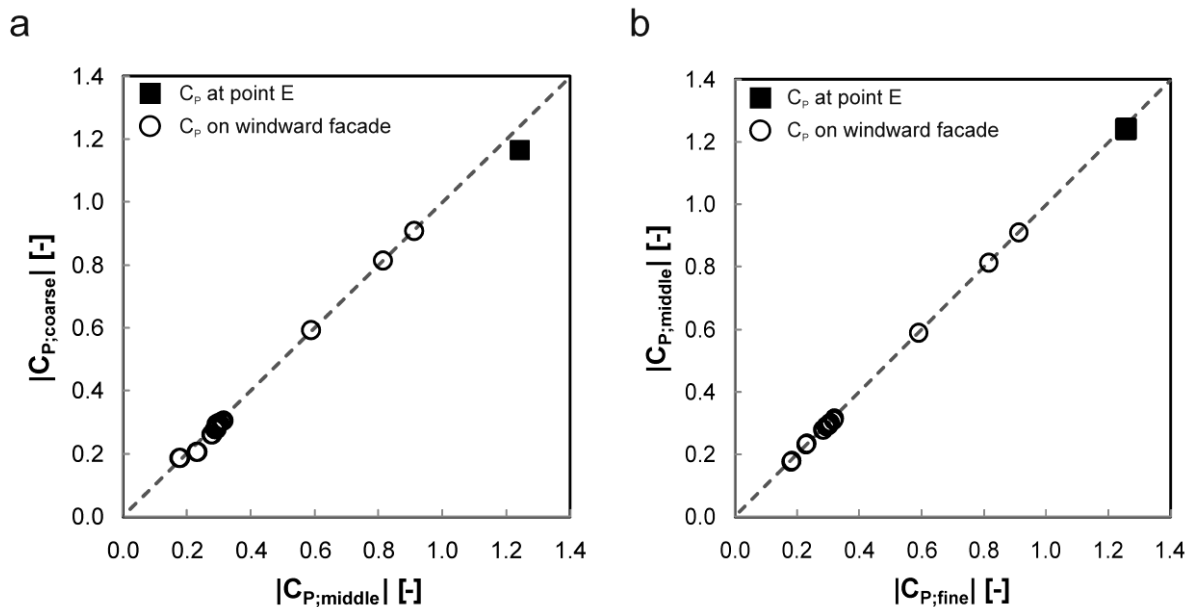


Figure 8. Grid-sensitivity analysis: comparison of pressure coefficients on windward facade and at position E in roof contraction with $c = 1$ m for different grids: (a) coarse grid versus middle grid and (b) middle grid versus fine grid.

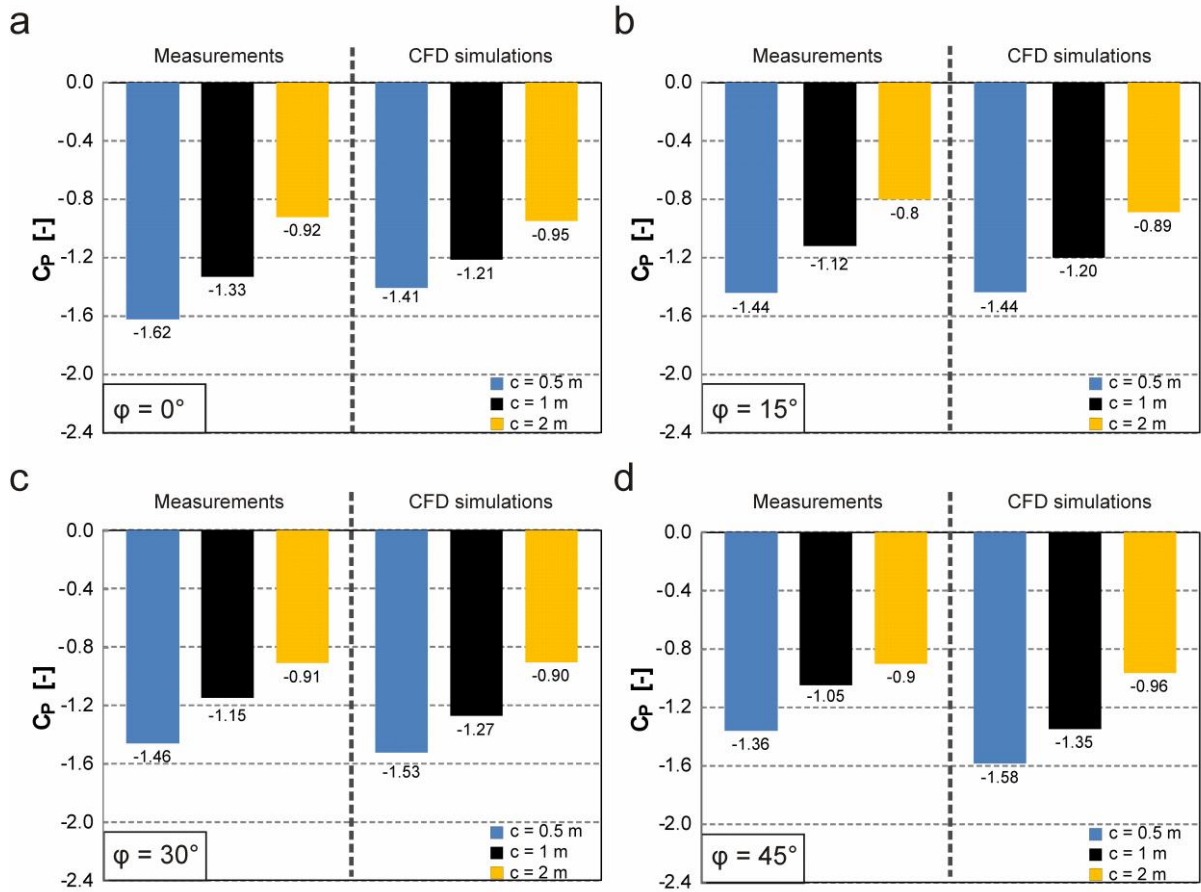


Figure 9. Experimental validation: comparison between measurements and CFD simulation results of pressure coefficients at position E for three contraction heights ($c = 0.5$ m, $c = 1$ m and $c = 2$ m) and four wind directions. (a) $\phi = 0^\circ$; (b) $\phi = 15^\circ$; (c) $\phi = 30^\circ$; (d) $\phi = 45^\circ$.

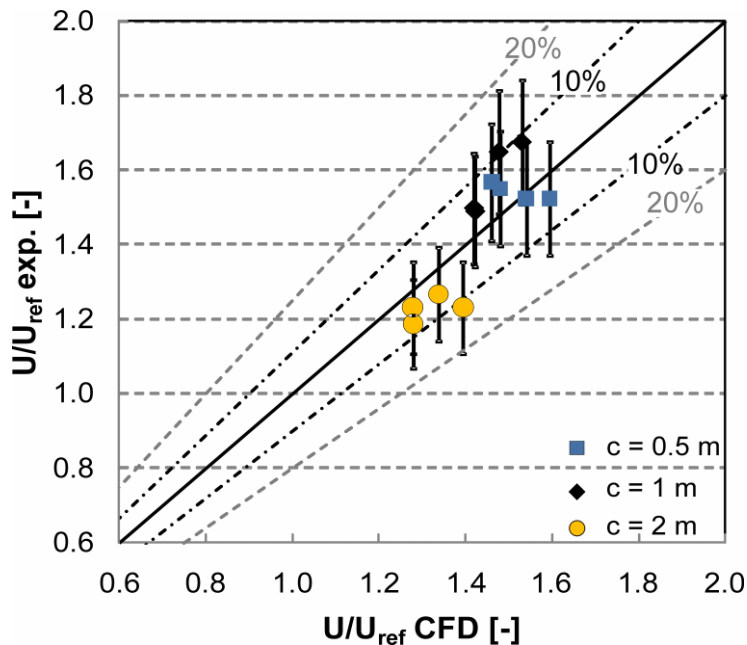


Figure 10. Experimental validation: comparison between measurements (exp.) and CFD simulation results of velocity ratio U/U_{ref} at mid-height in the centre of the roof contraction for three contraction heights ($c = 0.5$ m, $c = 1$ m and $c = 2$ m) and four wind directions ($\phi = 0^\circ$; 15° ; 30° ; 45°). The error bars represent the measuring accuracy of $\pm 10\%$.

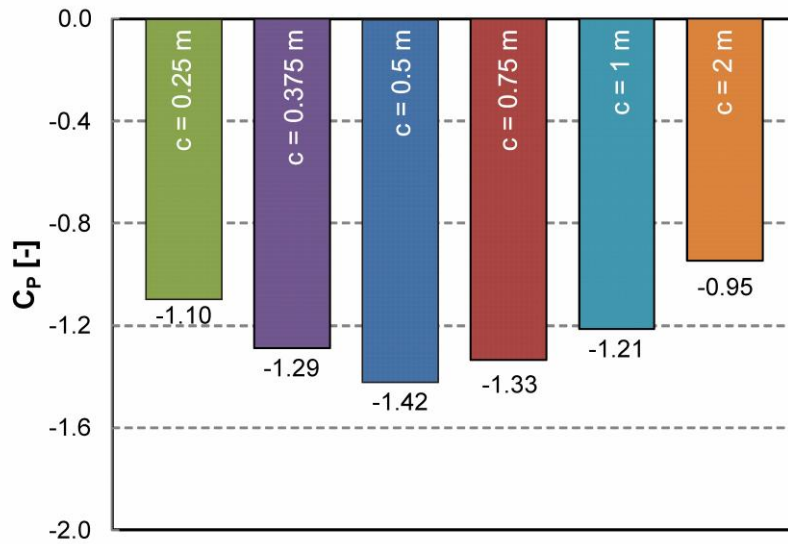


Figure 11. Optimisation results: mean pressure coefficients C_p at position E for wind direction $\varphi = 0^\circ$ and for six different values of the contraction height c . The largest negative pressure is obtained for $c = 0.5$ m.

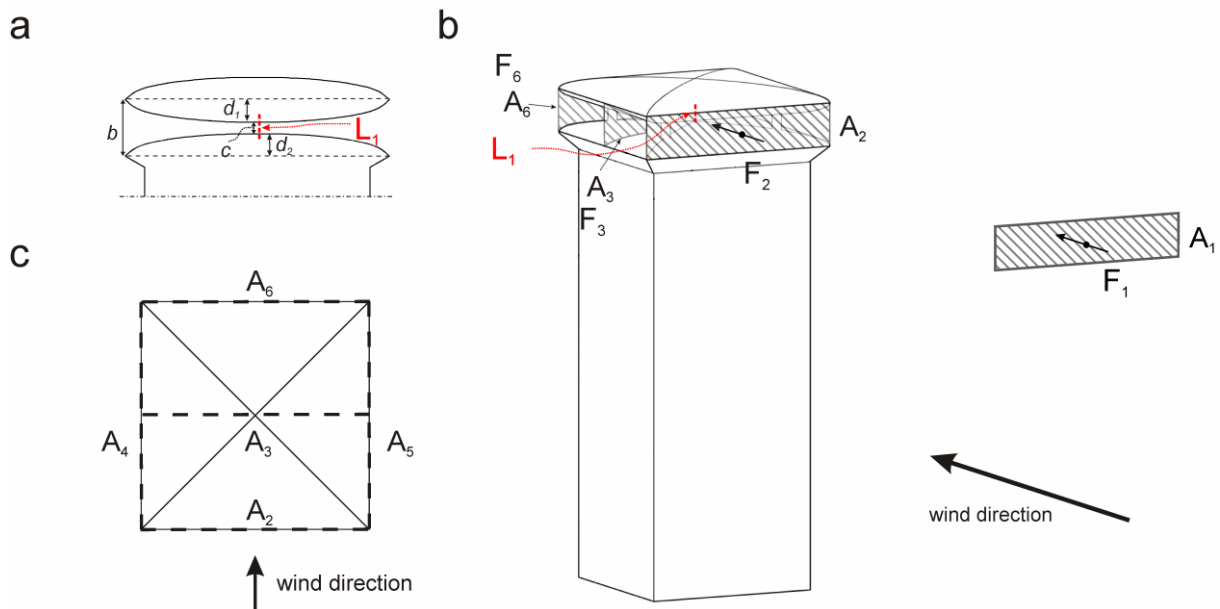


Figure 12. Definition of line segment, bounded planes and flow rates: (a) Vertical cross-section showing the vertical line segment L in the middle of the contraction. (b) Indication of the free-field plane A_1 and the roof vertical bounded planes A_2 , A_3 and A_6 and the vertical line segment L . (c) Top view of roof with indication of the roof vertical planes A_2 to A_6 .

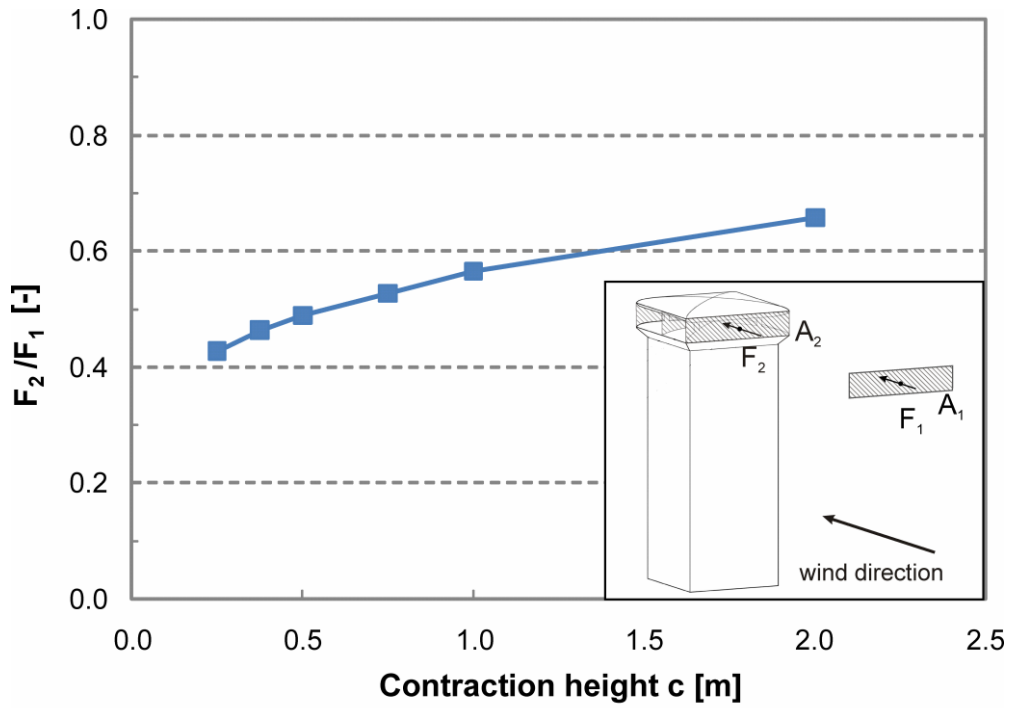


Figure 13. Ratio of flow rate F_2 (through inlet plane A_2) to flow rate F_1 (through free-field plane A_1) as a function of the contraction height c .

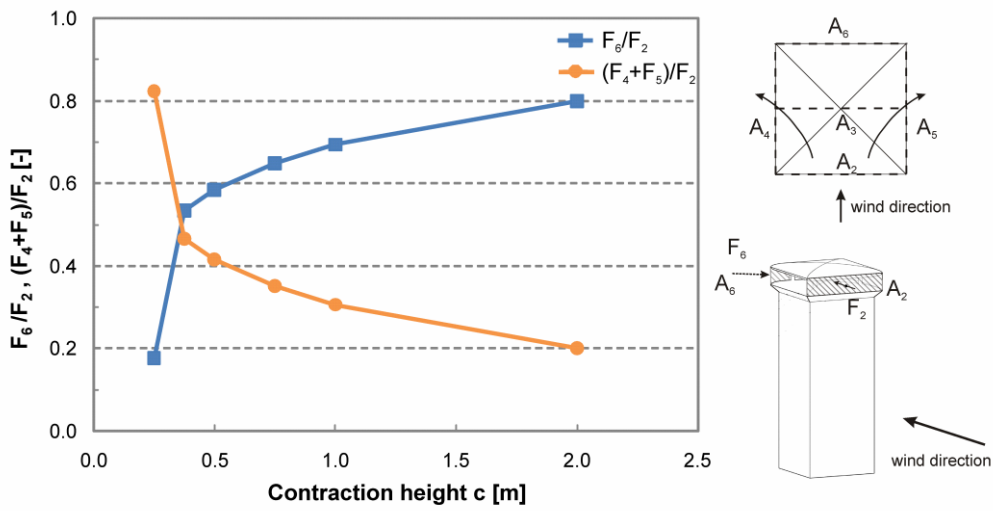


Figure 14. Ratio of F_6 (through roof outlet plane) to F_2 (through roof inlet plane) as function of the contraction height c and ratio of flow rates F_4+F_5 (through roof side planes) to flow rate F_2 . The sum of the two curves is equal to one.

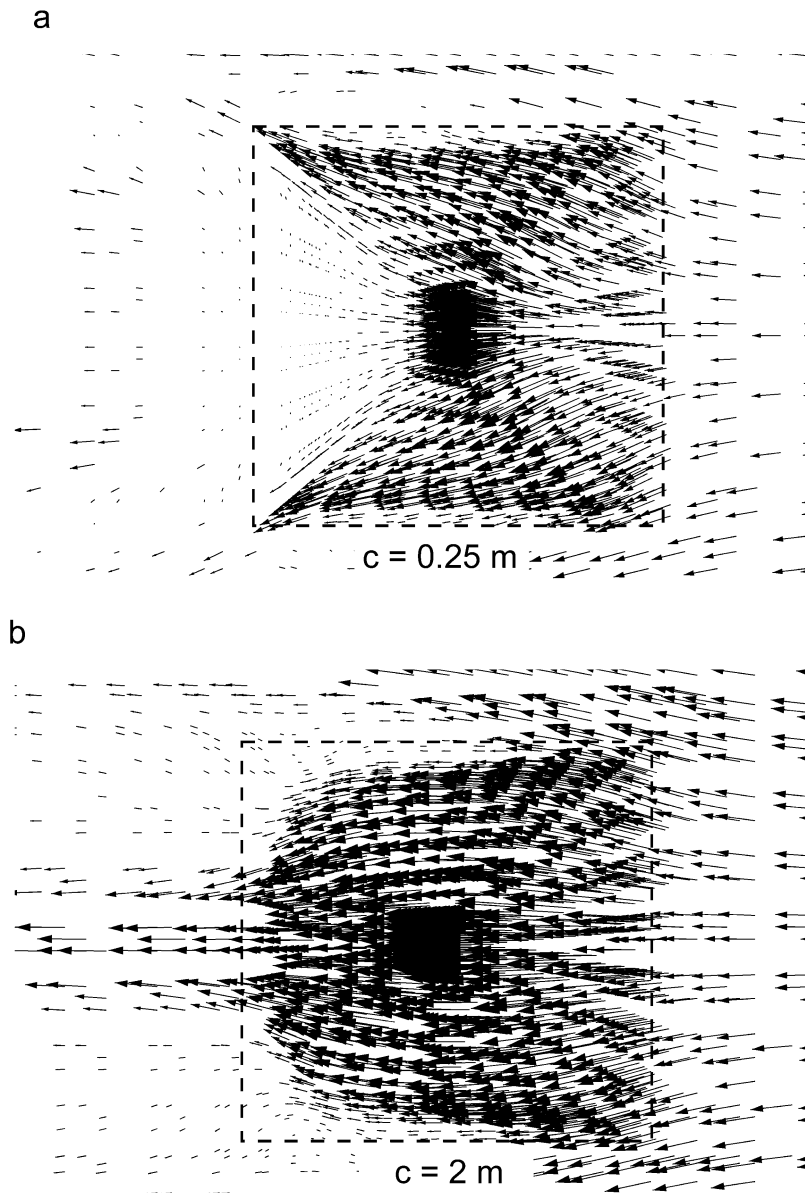


Figure 15. Velocity vectors in a horizontal plane in the middle of the roof contraction for $\varphi = 0^\circ$ and for (a) $c = 0.25$ m and (b) $c = 2$ m, illustrating the presence of a strong wind-blocking effect for lower c -values.

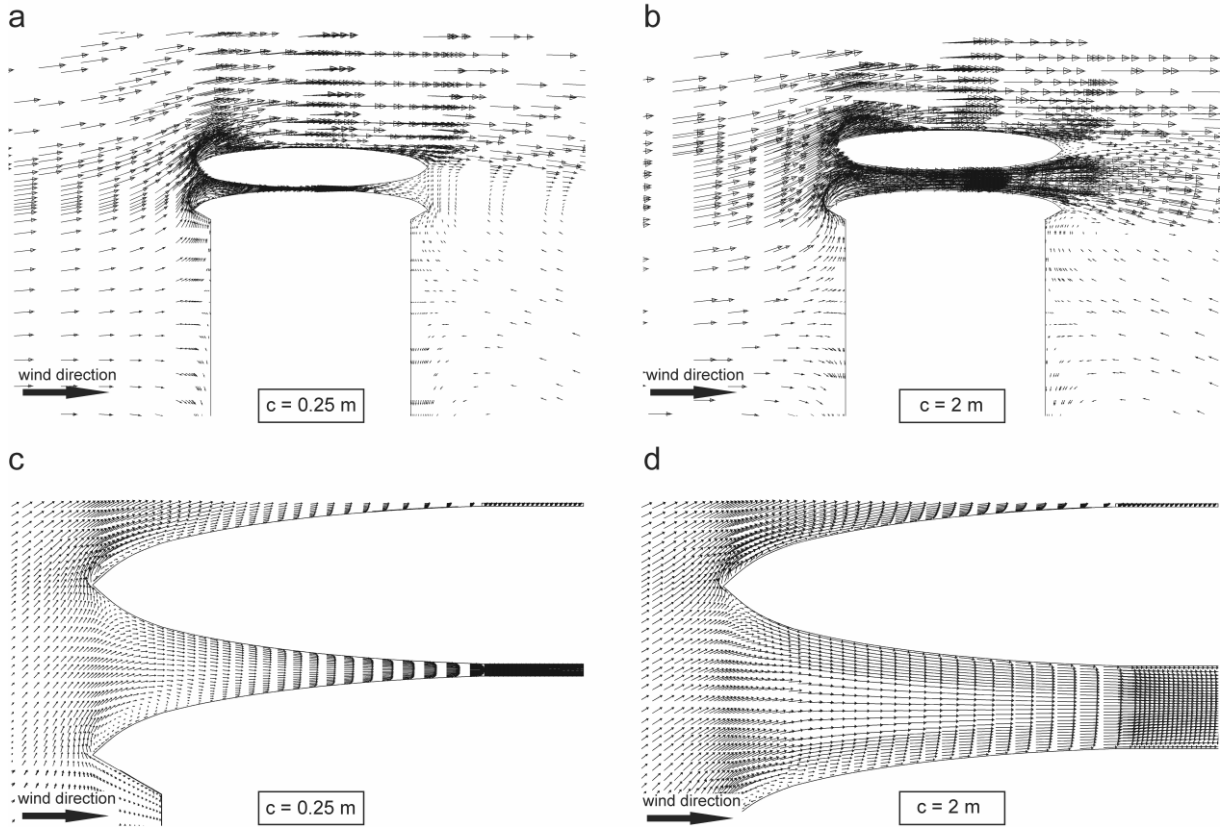


Figure 16. Velocity vectors in the vertical centre plane for $\phi = 0^\circ$, illustrating the presence of a strong wind-blocking effect for lower c -values; (a) $c = 0.25$ m; (b) $c = 2$ m; (c) $c = 0.25$ m; (d) $c = 2$ m.

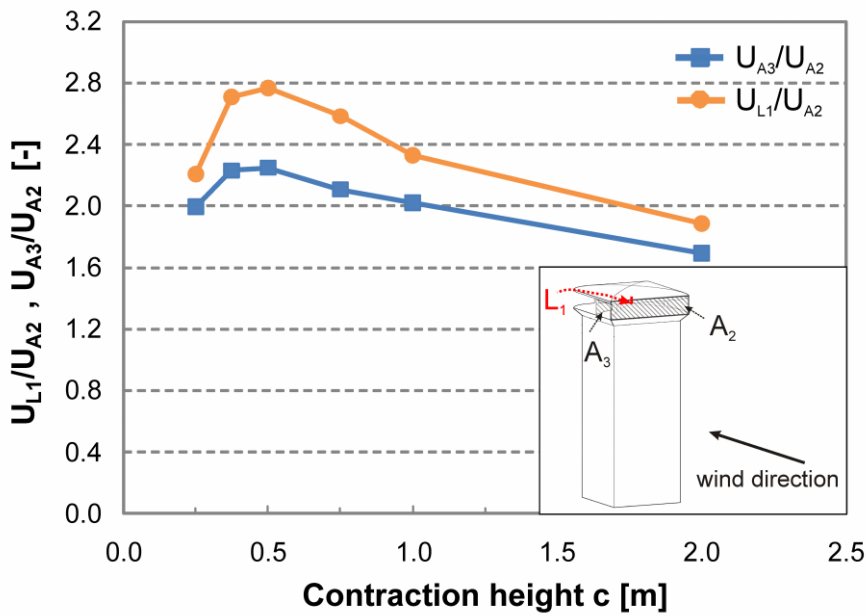


Figure 17. Average velocity ratios as function of the contraction height c : average velocity U_{A3} through plane A_3 to average velocity U_{A2} through A_2 , and average velocity U_{L1} along line segment L_1 to U_{A2} . The figure shows the acceleration of the flow due to the roof contraction. The highest acceleration is present for $c = 0.5$ m; both smaller and larger contraction heights result in smaller flow accelerations.